Extreme low-latitude TEC enhancement and GPS Scintillation at dawn

Sebastijan Mrak[1], Joshua Semeter[1], Yukitoshi Nishimura[1], and Anthea J. Coster[2]

[1]Department of Electrical and Computer Engineering and Center for Space Physics, Boston University, Boston, MA, USA
[2]Haystack Observatory, Massachusetts Institute of Technology, Westford, MA, USA

Key Points:

- GPS Scintillation abruptly arose at conjugate sunrise terminator during the storm recovery phase.
- Scintillation persisted for 5 hours over central America and decayed away within 2 hour after sunrise.
- Scintillation was co-located with a large TEC reaching more than twice of the day-side peak TEC.

Corresponding author: Sebastijan Mrak, smrak@bu.edu

Abstract

We report on an extreme density enhancement and scintillation at dawn, observed within the equatorial ionization anomaly (EIA) region, which was accompanied by a convective ionosphere storm (CIS). A region of Central America experienced an increase in total electron content (TEC) of up to ∼50 TECu, starting at a sunrise at the magnetic conjugate footpoints. The enhanced EIA expanded poleward and westward with the local sunrise terminator. Amplitude and phase scintillation at Global Positioning system (GPS) frequencies emerged with the TEC enhancement, and moved with the expanding EIA. The scintillation lasted for ∼5 hours, and decayed away in 2 hours after local sunrise.

Plain Language Summary

Low latitude ionosphere is conducive to a Rayleigh-Taylor instability inherent to the magnetic field lines parallel to the Earth. The instability's growth rate typically peaks after sunset, whereby an enhanced eastward electric field facilitates its growth. The instability promotes profound density depletion to rise to higher altitudes, whereby small scale irregularities develop. The resulting density irregularities are the most profound space weather threat to traversing radio signals. The timing of the scintillating signals follows the development of the instability. Namely, the most profound scintillation occurs in the pre-midnight sector, and it decays away in hours after midnight.

1 Introduction

Convective ionospheric storms (CIS) in the low-latitude ionosphere have been and continue to be a subject of intense theoretical and experimental studies. The CIS (Woodman & La Hoz, 1976; Ossakow & Chaturvedi, 1978; Hysell, 2000; Kelley et al., 2011) destabilizes ionospheric plasma near the magnetic equator by virtue of the Rayleigh-Taylor Instability (RTI). The instability facilitates the rise of plasma depletions (Equatorial Plasma bubbles, or EPB) that reach the topside ionosphere and then advect down along the field lines to the low-latitude ionosphere, stretching between the EIA peaks (Hysell, 2000; Groves et al., 1997). The EPBs consist of a large spatial spread of underlying density irregularities (Ossakow, 1981; Kelley et al., 2011, cf.), which profoundly affect traversing radiowaves by means of Fresnel diffraction off the irregularities at scales around $\sqrt{2\lambda Z}$ (λ being signal's wavelength, and Z distance from a receiver) (Kintner et al., 2007), that is about 400 m at the GPS frequencies.

A consequence of the Fresnel diffraction is a scintillating signal's amplitude (Yeh & Liu, 1982; Basu et al., 1988; Groves et al., 1997), with a peculiar local time distribution which normally emerges after sunset, sometimes extending into the post-midnight sector (Basu et al., 1988; Béniguel et al., 2009; de Oliveira Moraes et al., 2017; Béniguel, 2019). The destabilizing driver that fosters the growth rate of the RTI and hence scintillation is eastward electric field at the equator. The field normally peaks after sunset – the pre-reversal enhancement (Farley et al., 1986) – whose strength is modulated by geomagnetic activity and seasonality (Fejer & Scherliess, 1997).

Sporadic observations and reports of EPB near pre-sunrise local times have been reported (Burke, 1979; Fukao et al., 2003; Zakharenkova et al., 2015; Wu et al., 2020); however, not much attention was given to these events, and our understanding of the impact on low-latitude TEC and scintillation is limited. A review of post-midnight EPBs points out that they preferentially occur during the geomagnetically quiet summer months of low solar activity (Otsuka, 2018). Nominal statistics of radio (primarily GPS) amplitude scintillation (Basu et al., 1988; Béniguel et al., 2009; Jiao & Morton, 2015; de Oliveira Moraes et al., 2017) do not capture these events due to low frequency. Furthermore, the pre-sunrise EPBs normally cannot scintillate the GPS signals due to low plasma density at this local time (e.g., Otsuka, 2018). On the other hand, some case studies (Fukao

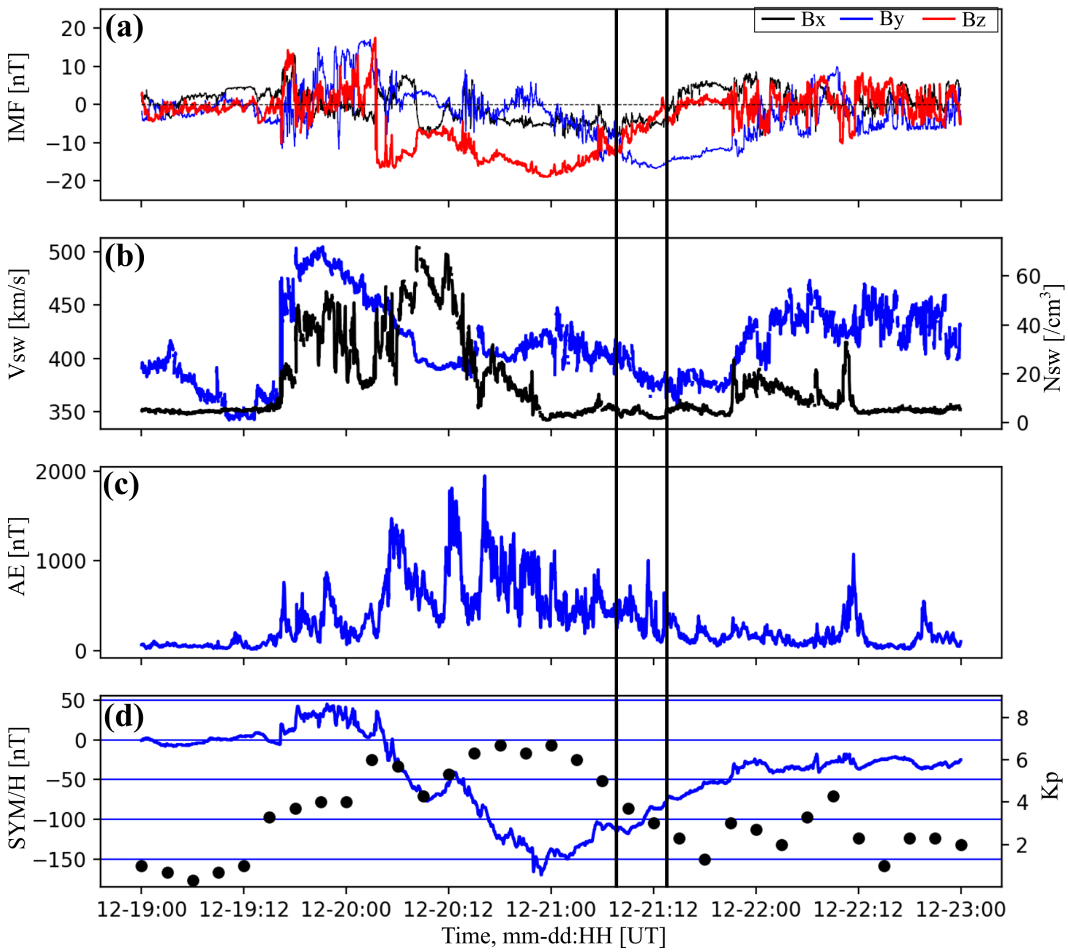

Figure 1. Solar wind and geomagnetic indices from the OMNIweb database. The time period under investigation is marked with vertical black lines. (a) Interplanetary magnetic field;. (b) Solar wind speed (blue) and density (black). (c) Auroral electrojet index. (d) Sym/H (blue) and Kp (black) indices.

et al., 2003; Zakharenkova et al., 2015; Wu et al., 2020) show dawn-time EPBs during winter months and geomagnetically disturbed days, just like the event we analyze in the remainder of this report. We analyze observations of an episodic plasma density enhancement accompanied by CIS, resulting in severe amplitude scintillation on the 21st December 2015. We present the 2-D structure from a network of 1-Hz UNAVCO GPS receivers in Central America and the Caribbean in the form of scintillation maps (Mrak et al., 2020). We find the scintillation emerged with the conjugate sunrise, and decayed a few hours after the local sunrise.

2 Observations

The GPS scintillation event occurred during the geomagnetically active period, as depicted in Figure 1. A high-speed solar wind with a northward oriented interplanetary magnetic field (IMF) hit the magnetopause on the 19 December 2015. The IMF turned southward on the next day, fueling a geomagnetic storm intensification indicated by the SYM/H index. The storm reached its peak with SYM/H≈-150 nT and the Planetary

K index (Kp) reaching 7^-. The storm's main phase was accompanied by several intense substorm intensifications, indicated by the Auroral Electrojet (AE) index exceeding 1000 nT. The IMF remained southward for about 30 hours. The scintillation event described below was recorded in the American longitude sector, and it occurred in the storm recovery period, indicated by the two vertical lines. The IMF rotated from predominantly southward (negative Bz) to the dusk-to-dawn direction (negative By).

We utilize 1-second UNAVCO GPS receivers located at low latitudes (below 30° geographic latitude GLAT) as scintillation monitors. We use modified scintillation indices to produce 2-D maps of scintillating irregularities. Due to the hardware limitations, we use Total Electron Content (TEC) to derive phase scintillation index σ_{TEC} (Beach & Kintner, 1999; Mrak et al., 2020), and amplitude scintillation index SNR_4 derived from carrier-to-noise ratio (CNR). While the former is defined as the usual phase scintillation index using standard deviation over 1 minute, the latter is computed in the same manner. The conventional normalization by mean intensity is avoided for the reasons discuss by Mrak et al. (2020).

$$\sigma_{TEC} = \sqrt{<\delta TEC^2> - <\delta TEC>^2} \tag{1}$$
$$SNR_4 = \sqrt{<\delta CNR^2> - <\delta CNR>^2} \tag{2}$$

where $<\cdot>$ is a temporal average operation, and δ denotes a high-pass filtered quantity with a cut-off frequency of 0.1 Hz. The line-of-sight scintillation index was converted to vertical via mapping function upon calculation (Spogli et al., 2009). We use the traditional scintillation index S_4 on a single receiver to demonstrate the scintillation intensity. Totally 38 receivers were available during the storm period, with spatial distribution depicted by the magenta markers in Figure 2a. We utilize available spatial distribution of the receivers and construct scintillation maps in Figure 2 using the method described by (Mrak et al., 2020). The underlying TEC maps were obtained from the MIT Haystack GPS-TEC data product (Vierinen et al., 2016).

We present a sequence of the scintillation maps around sunrise in Figure 2. The cyan solid line in the maps denotes the local sunrise terminator at 350 km altitude. In contrast, a dashed blue line is a magnetic conjugate location of the sunrise terminator mapped from the southern hemisphere, hereafter referred to as the conjugate sunrise terminator. We refer to the conjugate sunlit region as that being between the conjugate sunrise terminator and local sunrise terminator. In this case we are referring to the northern hemisphere as marked in Figure 2b. The scintillation maps include locations and median values of amplitude scintillation index (red dots) recorded within 15 minutes prior to the panel's epoch. Scintillation indicators are overlaid on top of TEC maps. The EIA is clearly seen in the northern hemisphere, lingering over central America near 20°MLAT. The scintillation emerged with the conjugate sunrise terminator (Figure 2b), within the EIA. The scintillation area remained within the EIA, fixed in geographic location, for a duration of the conjugate sunlit (panels b – d). The region of scintillation then rapidly expanded poleward and westward at the time of local sunrise terminator. The expansion took place together with the expansion of the EIA. This expansion was accompanied by intensification of scintillation. The scintillation then slowly decayed as TEC decreased in two hours after the local sunrise. A video with a 5-minute resolution is available as supplemental material (Movie S1).

Total scintillation occurrence and strength as a function of Universal Time (UT), and Magnetic Local Time (MLT) is presented in Figure 3. We plot network-wide lines-of-sight-average scintillation indices ($<\cdot>$) multiplied by the total number of recorded scintillation events N at any given time. Two distinct scintillation intensifications stand out as a function of UT, per the scintillation maps. The first peak corresponds to a period of conjugate sunrise, whereas the second intensification took off with the local sunrise. The area over central America was affected by this exceptional space weather phenomenon for a total of ~5 hours. The bottom panel shows scintillation indices as a func-

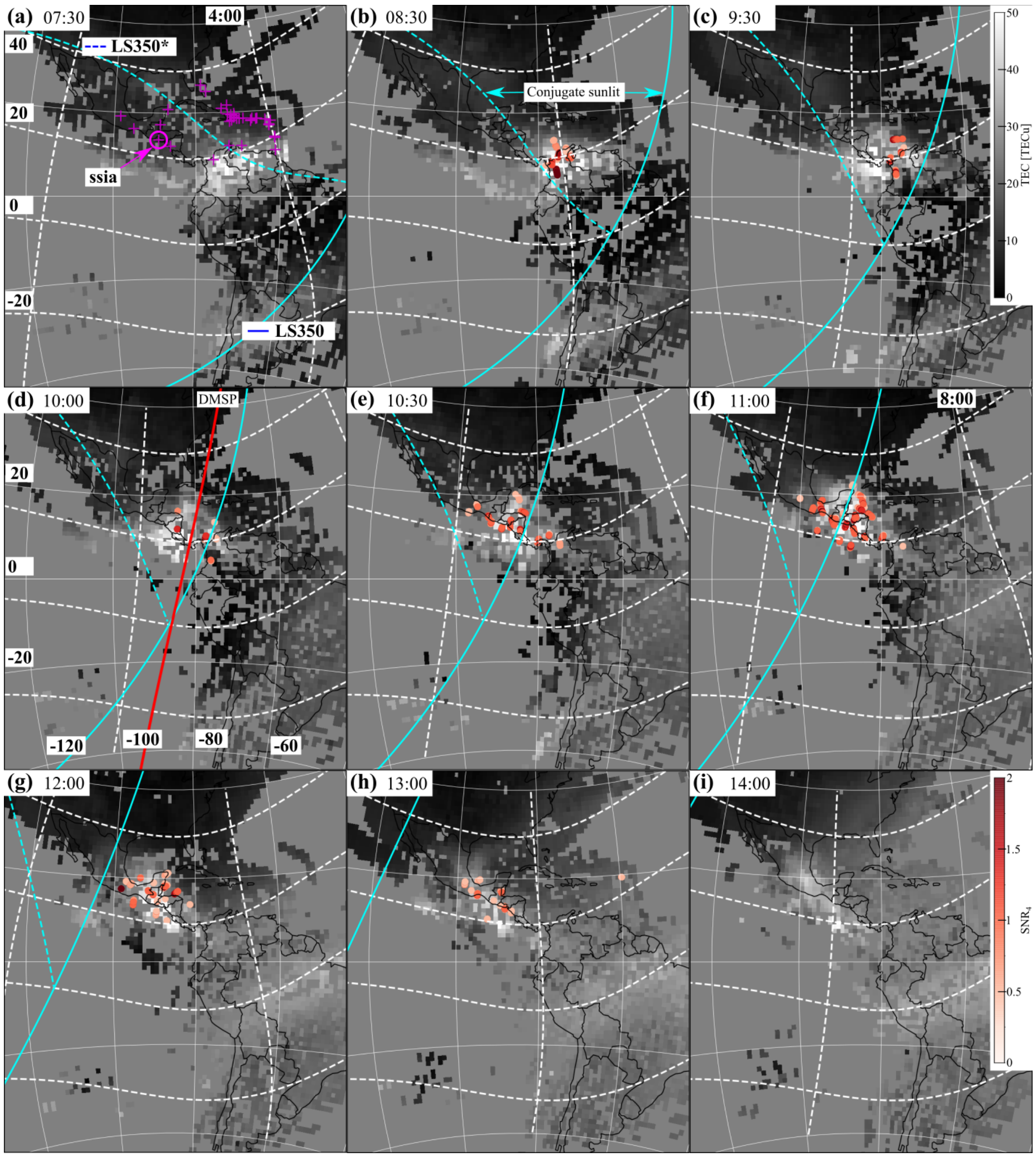

Figure 2. (a–i) Scintillation maps depicting location and strength of amplitude scintillation index SNR_4 as red dots. The solid cyan line is the local sunrise terminator at 350 km altitude, and the dashed blue line is the conjugate sunrise terminator (see text for details). Panel (a) depicts locations of the 1-Hz GPS receivers (magenta markers). Panel (c) includes red line fiducial, representing the DMSP F16 trajectory. (g) Receivers' averaged and normalized time-series presentation of amplitude (red) and phase (black) scintillation (see text for details). Continuous lines are for the event, whereas markers denote scintillation measured on 18th December 2015.

tion of MLT, whereby locations of ionospheric piercing points were converted to geomagnetic coordinates. The scintillation emerged right before 4 MLT and decayed away by 9 MLT.

We compare this event with a control day which was chosen to be the most geomagnetically quiet day before this storm – 18th December 2015. This control day is convenient baseline as the receivers did measure weak scintillation, at local time that well

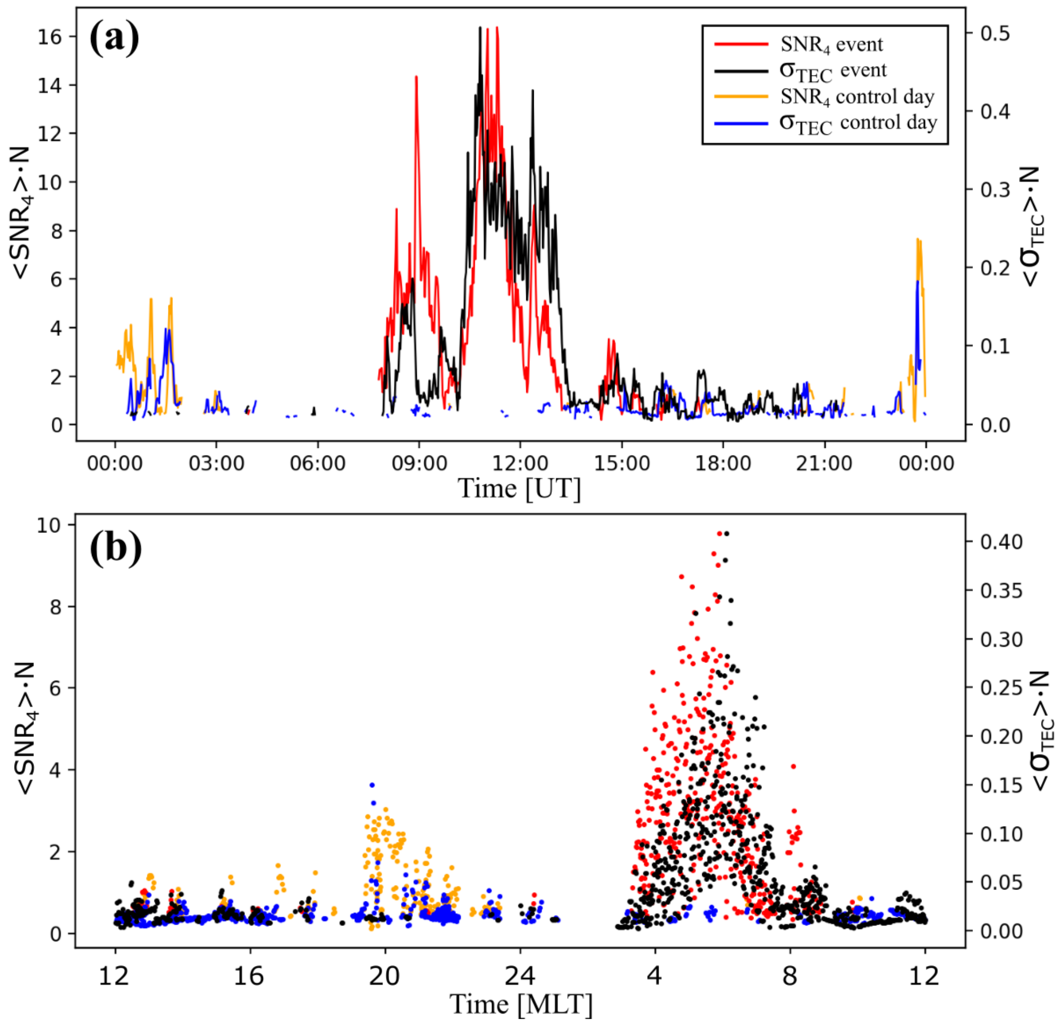

Figure 3. Time-series plots of median scintillation index receiver-averaged and normalized time-series presentation of amplitude (red) and phase (black) scintillation (see text for details). Continuous lines are for the event, whereas markers denote scintillation measured on 18th December 2015.

fits the climatology. Namely, the scintillation persisted for a couple of hours, beginning near 19 MLT. There is a distinct time shift between the events, which pictorially bolster anomalous timing.

We examine this phenomenon from a single receiver (SSIA, Honduras 89.12°W, 13.7°N) point-of-view, located underneath the scintillation region between ∼10 − 13 UT. We plot vertical TEC (vTEC) from this receiver over the day in Figure 4a. We convert slant TEC to vTEC via differential receiver bias estimation based on the minimization of standard deviation (Ma & Maruyama, 2003). The thick blue line is average vTEC over lines-of-sight above 30-degree elevation angle. For comparison, averaged vTEC measured on 18th December (the control day) is plotted as the red line for a comparison. Local sunrise times are marked for the receiver location. The TEC enhancement began at the time of conjugate sunrise (LS350*), with a total TEC increase from ∼10 to ∼50 TEC units (TECu, 1 TECu=10^{16} electrons per square meter). Large perturbations in the vTEC started developing before a local sunrise terminator at 350 km (LS350). The perturbations decayed

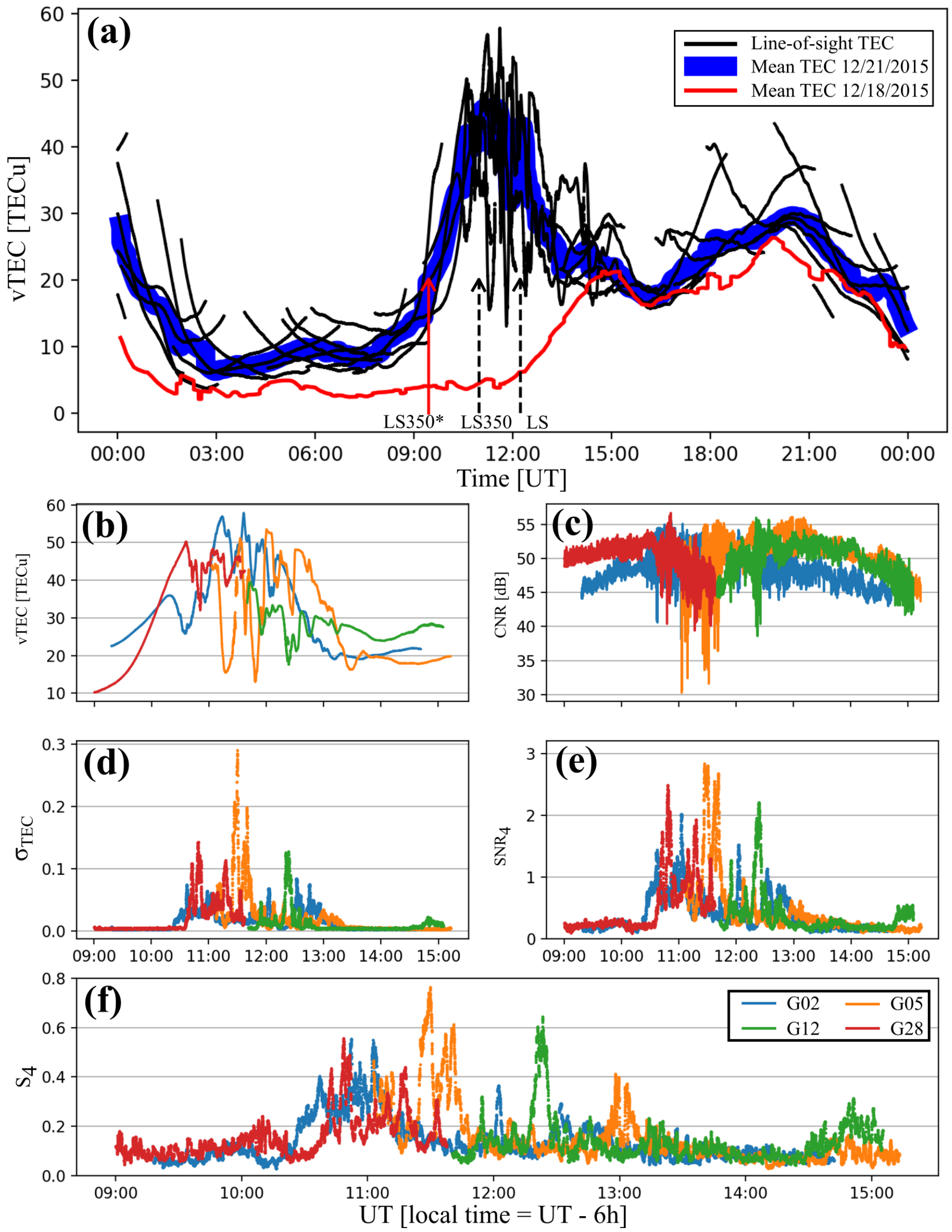

Figure 4. Data derived from SSIA receiver located in Honduras. (a) Vertical TEC on the day of the event for individual GPS satellites above 30 deg elevation (black), the blue line is averaged vTEC, and the red line is averaged vTEC on 18th December 2015. Markers denote sunrises (description in text). (b–e) Parameter estimates for four GPS satellites: (b) vTEC, (c) carrier-to-noise ratio CNR, (d) phase scintillation index σ_{TEC}, (e) amplitude scintillation index SNR_4. (f) Conventional amplitude scintillation index S_4 for reference.

away together with decreasing background TEC starting at the local sunrise at the ground (LS). Remarkably, the total TEC reached a daily peak at the sunrise, exceeding a normal daily daytime peak.

We show the four most affected lines-of-sight in panels b-f of Figure 4. TEC depletions within the anomalous enhancement exceeded 30 TECu. They had embedded

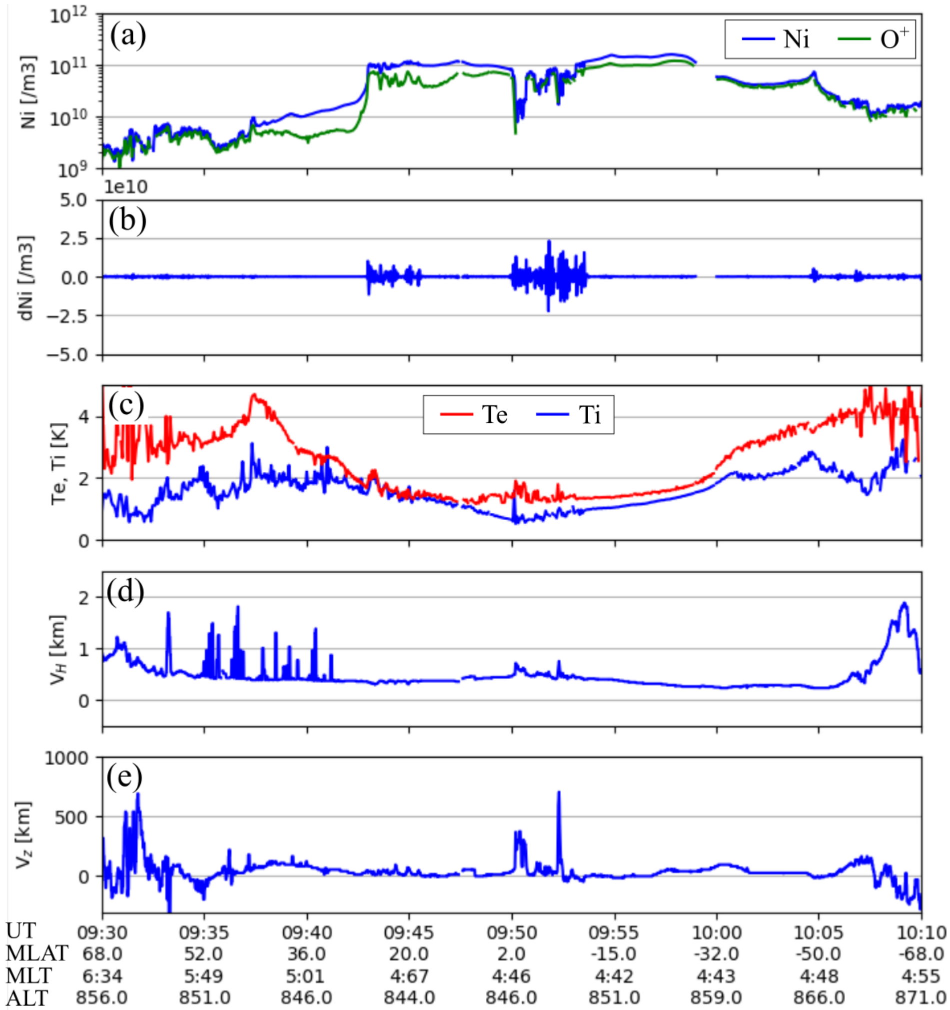

Figure 5. DMSP F16 measurements of plasma parameters during a recorded scintillation time period. (a) Ion density, (b) 0.1 Hz high-pass filtered ion density, (c) Electron (Te) and ion (Ti) temperatures, (d) horizontal (cross-track) ion drift (positive sunward), (e) vertical ion drift (positive up).

smaller perturbations with noticeable data gaps marking losses of signal. In panel (c), huge variations in CNR are co-linear with the TEC depletions, with fades exceeding 10 dB. In the next row (d-e), the derived scintillation indices are presented, and in the bottom, the nominal scintillation index S_4 is presented as a reference. The S_4 was computed from the CNR, converted to intensity $I = 10^{CNR/10}$, and calculated as $S_4^2 = \sigma_I / < I >$ (i.e., Rodrigues & Moraes, 2019).

Lastly, the Defense Meteorological Space Program (DMSP) F16 traversed the anomalous density region in central America near 10 UT, with its trajectory drawn in Figure 2d. *In-situ* ion density, perpendicular ion flow components, and plasma temperatures are presented in Figure 5. This southbound pass encountered a sharp density gradient near 30°MLAT, with a total increase of about an order of magnitude. This occurred in the region where the GPS receivers measured the large TEC enhancement at dawn, reaching ∼50 TECu. Right within the region of enhanced plasma, plasma irregularities resided in the topside ionosphere (∼850 km), identified with a high-pass filtered (0.1 Hz) ion density (dNi) in the second panel. Another set of plasma irregularities were measured near the magnetic equator. Both irregularity regions were accompanied with subtle increase in ion and electron temperatures. Additionally, ion flow perturbations near the equator are positively correlated with the density irregularities, with a net eastward (sunward) horizontal flow (v_H), and upward flow (v_Z) of >100 m/s at the equator.

3 Discussion

Sporadic observations of EPB near sunrise have been reported (e.g., Fukao et al., 2003; Zakharenkova et al., 2015; Wu et al., 2020), but appear to be a rare phenomenon and is facilitated by magnetic activity. Although the exact timing and driving mechanism are ambiguous, the recent observations suggest they occur during a storm-time recovery phase in the winter hemisphere. Normal conditions for the RTI to operate is upward drift at the equator (Hysell, 2000; Martinis et al., 2005); however, normal condition at dawn is a westward electric field (Fejer & Scherliess, 1997), hence a zonal reversal is necessary for the RTI to operate. It has been shown that such reversals do occur at geomagnetically disturbed periods (Fejer et al., 1976; Bowman, 1978). Additionally, it has been speculated that in these kinds of circumstances, RTI could be operating together with the $\mathbf{E}\times\mathbf{B}$ instability (Burke, 1979). Long-lasting auroral activity drives the disturbance dynamo, which nudges the RTI with high efficiency in time delay below 12 hours and 20–30 hours (Scherliess & Fejer, 1997). Moreover, the disturbance dynamo effect peaks near 4:00 local time (Fejer et al., 1999). This is the local time we found the increase in scintillation (cf., Figure 3).

The presented event provides new insight in terms of preconditioning and timing of scintillation onset. We show that the EIA persisted throughout the night. Thus an uncharacteristically abundant plasma basin at low-latitudes (near 10–20° MLAT) lingered in the pre-dawn ionosphere. The initial onset of the scintillation, together with an episodic TEC increase, began at the conjugate sunrise. This observation is intriguing. Given the absence of abrupt changes in the solar wind or geomagnetic drivers during this period, we can think of only one catalyst for the plasma density increase and accompanying irregularity onset in the conjugate sunlit ionosphere – namely, conjugate photoelectron transport (Carlson, 1966). Further investigations are needed to determine whether the correlation with conjugate sunlight is causal or merely coincidental. We processed the scintillation data from 2012-2020, and this was the only event with such characteristics.

The scintillation strength and area increased significantly with local sunrise and expanded beyond 35°MLAT. The scintillation increase was accompanied by further TEC enhancement facilitated via photo-ionization, with the total TEC increase exceeding 50 TECu. Additionally, the EIA experienced sudden poleward expansion, an indication of an increased eastward electric field at the equator. This is expected based on the electric field diurnal pattern (Fejer & Scherliess, 1997), with an increased gradient (westward-to-eastward transition) during the geomagnetically disturbed period. The scintillation decayed away within two hours after the local sunrise, consistent with other reported observations (Fukao et al., 2003; Wu et al., 2020).

4 Summary

We presented an episodic increase in the EIA density, accompanied by GPS scintillation caused by a Convective Ionospheric Storm at dawn. The observations show that the EIA had persisted throughout the night, and became a region of scintillation-producing plasma irregularities with an onset at the conjugate sunrise terminator. The EIA density abruptly elevated to ∼50 TECu, and the scintillation severity followed the TEC trend. The EIA, as well as the scintillation, decayed within two hours after local sunrise, making the region experiencing severe space weather event for a total of ∼5 hours. We have placed the observation in context with other reports and deduced the following findings:

1. At dawn, EPBs appear to be characteristic of a storm recovery phase, observed at the local times when the disturbance dynamo is the most efficient.
2. The onset of the scintillation reported here was correlated with a local density increase beginning with the conjugate sunlit.
3. Scintillation increased at local sunrise, the region expands poleward and decayed away within a few hours.

A preliminary survey of scintillation occurrence in the American longitude sector between 2012-2020 shows that this was the only event with GPS scintillation at dawn local time.

Acknowledgments
The study was supported by NSF-AGS 1821135, NSF-AGS-1907698, NASA-0NSSC18K0657, and AFOSR FA9559-16-1-0364 awards to Boston University. GPS data is freely available at ftp://data-out.unavco.org/pub/highrate/1-Hz/rinex/. GPS TEC maps as well as DMSP data were retrieved from open madrigal database http://cedar.openmadrigal.org/. Solar wind and geomagnetic indices are available via https://cdaweb.sci.gsfc.nasa.gov/pub/data/omni/.

References

Basu, S., MacKenzie, E., & Basu, S. (1988, may). Ionospheric constraints on VHF/UHF communications links during solar maximum and minimum periods. *Radio Science*, *23*(3), 363–378. Retrieved from `http://doi.wiley.com/10.1029/RS023i003p00363` doi: 10.1029/RS023i003p00363

Beach, T. L., & Kintner, P. M. (1999, oct). Simultaneous Global Positioning System observations of equatorial scintillations and total electron content fluctuations. *Journal of Geophysical Research: Space Physics*, *104*(A10), 22553–22565. Retrieved from `http://doi.wiley.com/10.1029/1999JA900220` doi: 10.1029/1999JA900220

Béniguel, Y. (2019). Ionospheric Scintillations: Indices and Modeling. *Radio Science*, *54*(7), 618–632. doi: 10.1029/2018RS006655

Béniguel, Y., Adam, J. P., Jakowski, N., Noack, T., Wilken, V., Valette, J. J., . . . Arbesser-Rastburg, B. (2009). Analysis of scintillation recorded during the PRIS measurement campaign. *Radio Science*, *44*(5), 1–11. doi: 10.1029/2008RS004090

Bowman, G. (1978, jun). A relationship between polar magnetic substorms, ionospheric height rises and the occurrence of spread-F. *Journal of Atmospheric and Terrestrial Physics*, *40*(6), 713–722. Retrieved from `https://linkinghub.elsevier.com/retrieve/pii/0021916978901290` doi: 10.1016/0021-9169(78)90129-0

Burke, W. I. (1979). Plasma bubbles near the dawn terminator in the topside ionosphere. *Planetary and Space Science*, *27*(9), 1187–1193. doi: 10.1016/0032-0633(79)90138-7

Carlson, H. C. (1966, jan). Ionospheric heating by magnetic conjugate-point photoelectrons. *Journal of Geophysical Research*, *71*(1), 195–199. Retrieved from `http://doi.wiley.com/10.1029/JZ071i001p00195` doi: 10.1029/JZ071i001p00195

de Oliveira Moraes, A., Costa, E., Abdu, M. A., Rodrigues, F. S., de Paula, E. R., Oliveira, K., & Perrella, W. J. (2017). The variability of low-latitude ionospheric amplitude and phase scintillation detected by a triple-frequency GPS receiver. *Radio Science*, *52*(4), 439–460. doi: 10.1002/2016RS006165

Farley, D. T., Bonelli, E., Fejer, B. G., & Larsen, M. F. (1986). The prereversal enhancement of the zonal electric field in the equatorial ionosphere. *Journal of Geophysical Research*, *91*(A12), 13723. Retrieved from http://doi.wiley.com/10.1029/JA091iA12p13723 doi: 10.1029/JA091iA12p13723

Fejer, B. G., Farley, D. T., Balsley, B. B., & Woodman, R. F. (1976, sep). Radar studies of anomalous velocity reversals in the equatorial ionosphere. *Journal of Geophysical Research*, *81*(25), 4621–4626. Retrieved from http://doi.wiley.com/10.1029/JA081i025p04621 doi: 10.1029/JA081i025p04621

Fejer, B. G., & Scherliess, L. (1997, nov). Empirical models of storm time equatorial zonal electric fields. *Journal of Geophysical Research: Space Physics*, *102*(A11), 24047–24056. Retrieved from http://doi.wiley.com/10.1029/97JA02164 doi: 10.1029/97JA02164

Fejer, B. G., Scherliess, L., & de Paula, E. R. (1999, sep). Effects of the vertical plasma drift velocity on the generation and evolution of equatorial spread F. *Journal of Geophysical Research: Space Physics*, *104*(A9), 19859–19869. Retrieved from http://doi.wiley.com/10.1029/1999JA900271 doi: 10.1029/1999JA900271

Fukao, S., Ozawa, Y., Yamamoto, M., & Tsunoda, R. T. (2003, nov). Altitude-extended equatorial spread F observed near sunrise terminator over Indonesia. *Geophysical Research Letters*, *30*(22), 3–6. Retrieved from http://doi.wiley.com/10.1029/2003GL018383 doi: 10.1029/2003GL018383

Groves, K. M., Basu, S., Weber, E. J., Smitham, M., Kuenzler, H., Valladares, C. E., ... Kendra, M. J. (1997, sep). Equatorial scintillation and systems support. *Radio Science*, *32*(5), 2047–2064. Retrieved from http://doi.wiley.com/10.1029/97RS00836 doi: 10.1029/97RS00836

Hysell, D. (2000, aug). An overview and synthesis of plasma irregularities in equatorial spread F. *Journal of Atmospheric and Solar-Terrestrial Physics*, *62*(12), 1037–1056. Retrieved from https://linkinghub.elsevier.com/retrieve/pii/S136468260000095X doi: 10.1016/S1364-6826(00)00095-X

Jiao, Y., & Morton, Y. T. (2015, sep). Comparison of the effect of highlatitude and equatorial ionospheric scintillation on GPS signals during the maximum of solar cycle 24. *Radio Science*, *50*(9), 886–903. Retrieved from https://onlinelibrary.wiley.com/doi/abs/10.1002/2015RS005719 doi: 10.1002/2015RS005719

Kelley, M. C., Makela, J. J., de La Beaujardière, O., & Retterer, J. (2011, jun). Convective Ionospheric Storms: A Review. *Reviews of Geophysics*, *49*(2), RG2003. Retrieved from http://doi.wiley.com/10.1029/2010RG000340 doi: 10.1029/2010RG000340

Kintner, P. M., Ledvina, B. M., & de Paula, E. R. (2007, sep). GPS and ionospheric scintillations. *Space Weather*, *5*(9), n/a–n/a. Retrieved from http://doi.wiley.com/10.1029/2006SW000260http://files/178/rds1552.pdfhttp://files/248/rds1992.pdfhttp://files/247/swe177.pdf doi: 10.1029/2006SW000260

Ma, G., & Maruyama, T. (2003). Derivation of TEC and estimation of instrumental biases from GEONET in Japan. *Annales Geophysicae*, *21*(10), 2083–2093. Retrieved from www.ann-geophys.net/21/2083/2003/angeo-21-2083-2003http://www.ann-geophys.net/21/2083/2003/ doi: 10.5194/angeo-21-2083-2003

Martinis, C. R., Mendillo, M., & Aarons, J. (2005). Toward a synthesis of equatorial spread F onset and suppression during geomagnetic storms. *Journal of Geophysical Research*, *110*(A7), A07306. Retrieved from http://doi.wiley.com/10.1029/2003JA010362 doi: 10.1029/2003JA010362

Mrak, S., Semeter, J., Nishimura, Y., Rodrigues S., F., & Groves, K. (2020). Leveraging geodetic GPS receivers for ionospheric scintillation science. *Radio Science*. doi: doi.org/10.1002/essoar.10503102.1

Ossakow, S. L. (1981, may). Spread-F theoriesa review. *Journal of Atmospheric and Terrestrial Physics*, *43*(5-6), 437–452. Retrieved from https://linkinghub.elsevier.com/retrieve/pii/0021916981901070 doi: 10.1016/0021-9169(81)90107-0

Ossakow, S. L., & Chaturvedi, P. K. (1978). Morphological studies of rising equatorial spread F bubbles. *Journal of Geophysical Research*, *83*(A5), 2085. Retrieved from http://doi.wiley.com/10.1029/JA083iA05p02085 doi: 10.1029/JA083iA05p02085

Otsuka, Y. (2018, dec). Review of the generation mechanisms of post-midnight irregularities in the equatorial and low-latitude ionosphere. *Progress in Earth and Planetary Science*, *5*(1), 57. Retrieved from https://progearthplanetsci.springeropen.com/articles/10.1186/s40645-018-0212-7 doi: 10.1186/s40645-018-0212-7

Rodrigues, F. S., & Moraes, A. O. (2019). ScintPi: A Low-Cost, Easy-to-Build GPS Ionospheric Scintillation Monitor for DASI Studies of Space Weather, Education, and Citizen Science Initiatives. *Earth and Space Science*, *6*(8), 1547–1560. doi: 10.1029/2019EA000588

Scherliess, L., & Fejer, B. G. (1997, nov). Storm time dependence of equatorial disturbance dynamo zonal electric fields. *Journal of Geophysical Research: Space Physics*, *102*(A11), 24037–24046. Retrieved from http://doi.wiley.com/10.1029/97JA02165 doi: 10.1029/97JA02165

Spogli, L., Alfonsi, L., De Franceschi, G., Romano, V., Aquino, M. H. O., & Dodson, A. (2009, sep). Climatology of GPS ionospheric scintillations over high and mid-latitude European regions. *Annales Geophysicae*, *27*(9), 3429–3437. Retrieved from https://www.ann-geophys.net/27/3429/2009/ doi: 10.5194/angeo-27-3429-2009

Vierinen, J., Coster, A. J., Rideout, W. C., Erickson, P. J., & Norberg, J. (2016). Statistical framework for estimating GNSS bias. *Atmospheric Measurement Techniques*, *9*(3), 1303–1312. doi: 10.5194/amt-9-1303-2016

Woodman, R. F., & La Hoz, C. (1976, nov). Radar observations of F region equatorial irregularities. *Journal of Geophysical Research*, *81*(31), 5447–5466. Retrieved from http://doi.wiley.com/10.1029/JA081i031p05447 doi: 10.1029/JA081i031p05447

Wu, K., Xu, J., Yue, X., Xiong, C., Wang, W., Yuan, W., ... Luo, J. (2020). Equatorial plasma bubbles developing around sunrise observed by an all-sky imager and global navigation satellite system network during storm time. *Annales Geophysicae*, *38*(1), 163–177. doi: 10.5194/angeo-38-163-2020

Yeh, K. C., & Liu, C.-H. (1982). Radio wave scintillations in the ionosphere. *Proceedings of the IEEE*, *70*(4), 324–360. Retrieved from https://ieeexplore.ieee.org/document/1456581 doi: 10.1109/PROC.1982.12313

Zakharenkova, I., Astafyeva, E., & Cherniak, I. (2015, oct). Early morning irregularities detected with spaceborne GPS measurements in the topside ionosphere: A multisatellite case study. *Journal of Geophysical Research: Space Physics*, *120*(10), 8817–8834. Retrieved from http://doi.wiley.com/10.1002/2015JA021447 doi: 10.1002/2015JA021447

Figure 1.

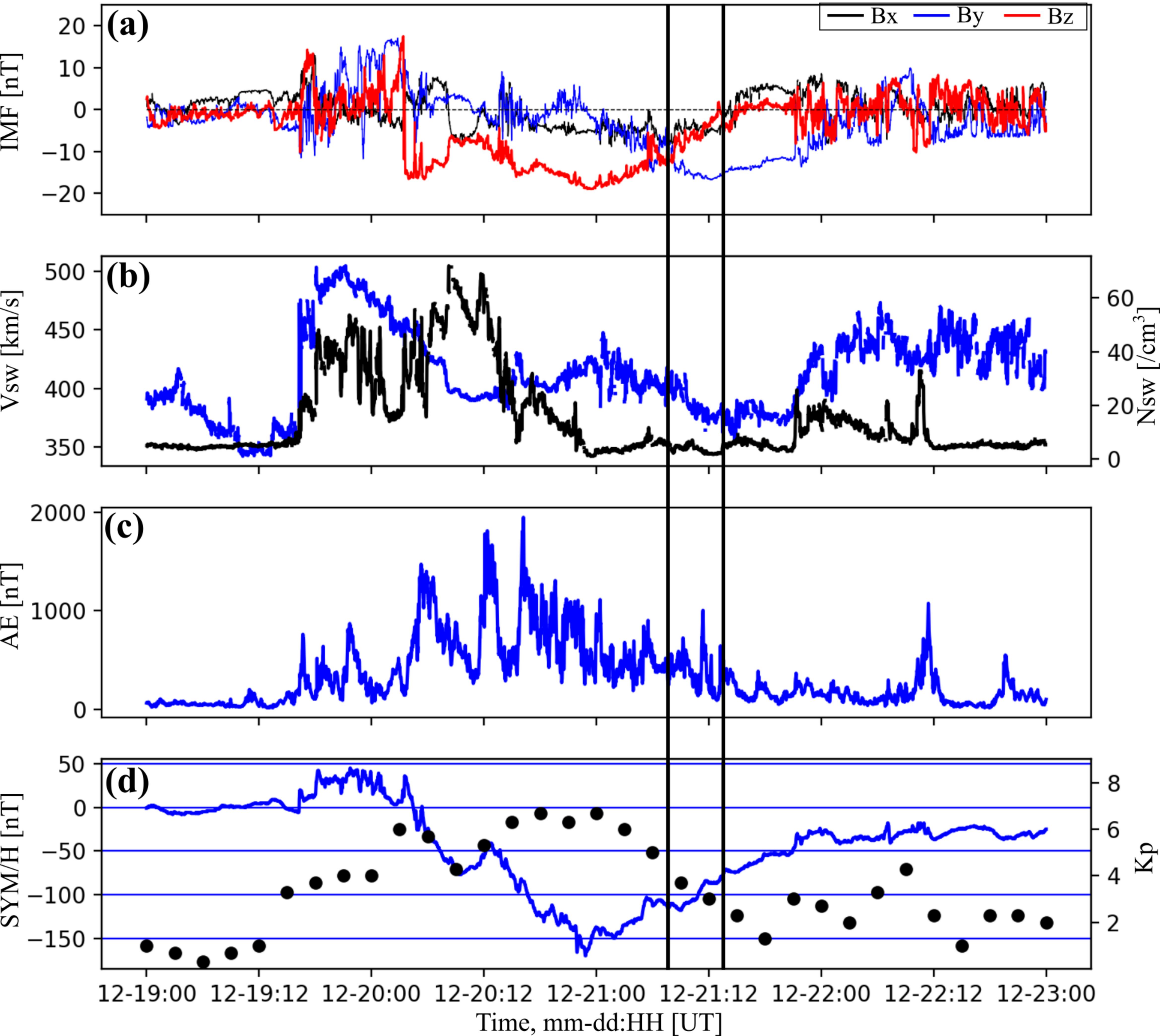
(a)
Bx
By
Bz
IMF [nT]
(b)
Vsw [km/s]
Nsw [/cm^3]
(c)
AE [nT]
(d)
SYM/H [nT]
Kp
12-19:00
12-19:12
12-20:00
12-20:12
12-21:00
12-21:12
12-22:00
12-22:12
12-23:00
Time, mm-dd:HH [UT]

Figure 2.

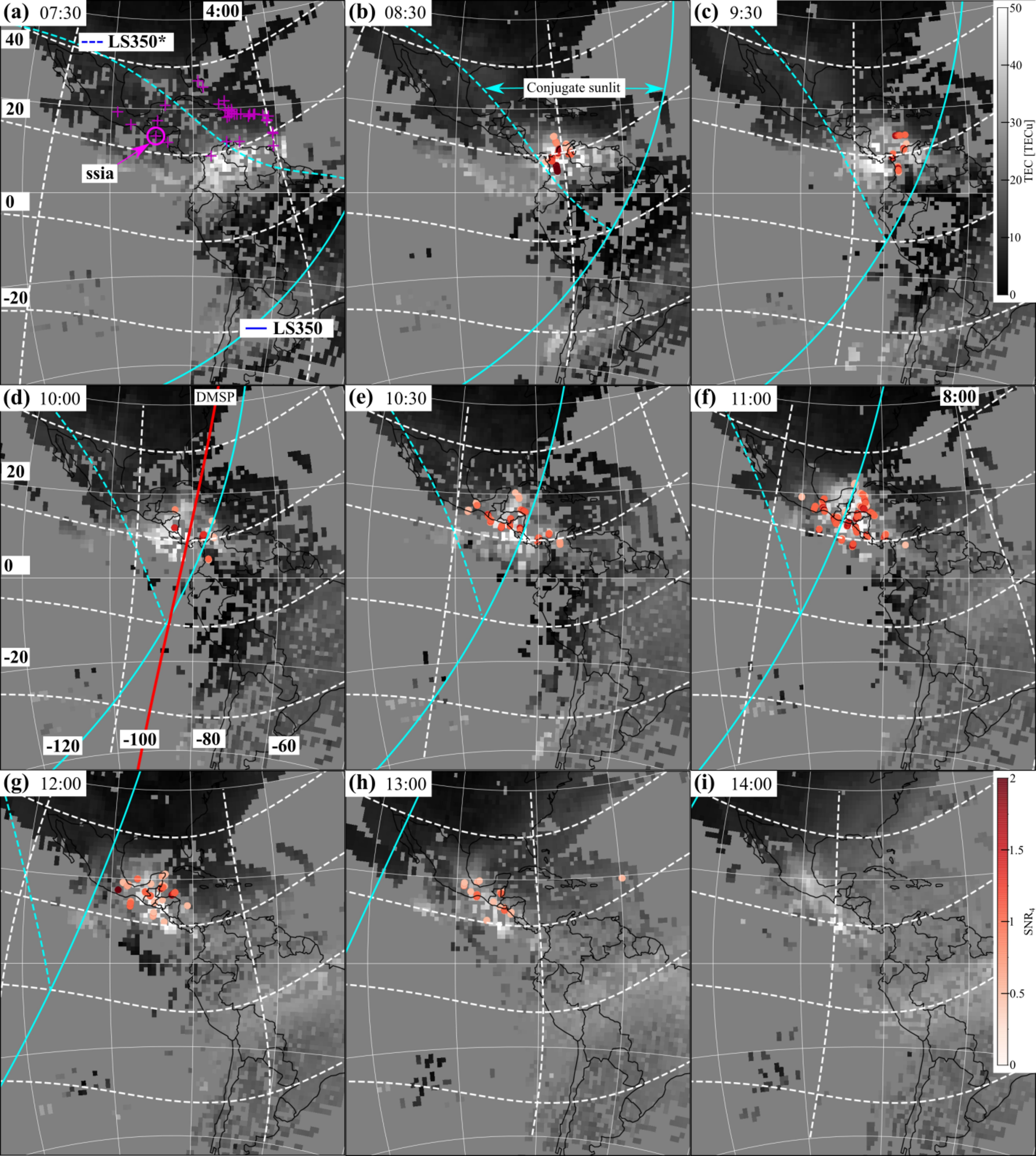

(a) 07:30
4:00
40
20
0
-20
LS350*
LS350
ssia
(b) 08:30
Conjugate sunlit
(c) 9:30
TEC [TECu]
50
40
30
20
10
0
(d) 10:00
DMSP
-120
-100
-80
-60
(e) 10:30
(f) 11:00
8:00
(g) 12:00
(h) 13:00
(i) 14:00
SNR_4
2
1.5
1
0.5
0

Figure 3.

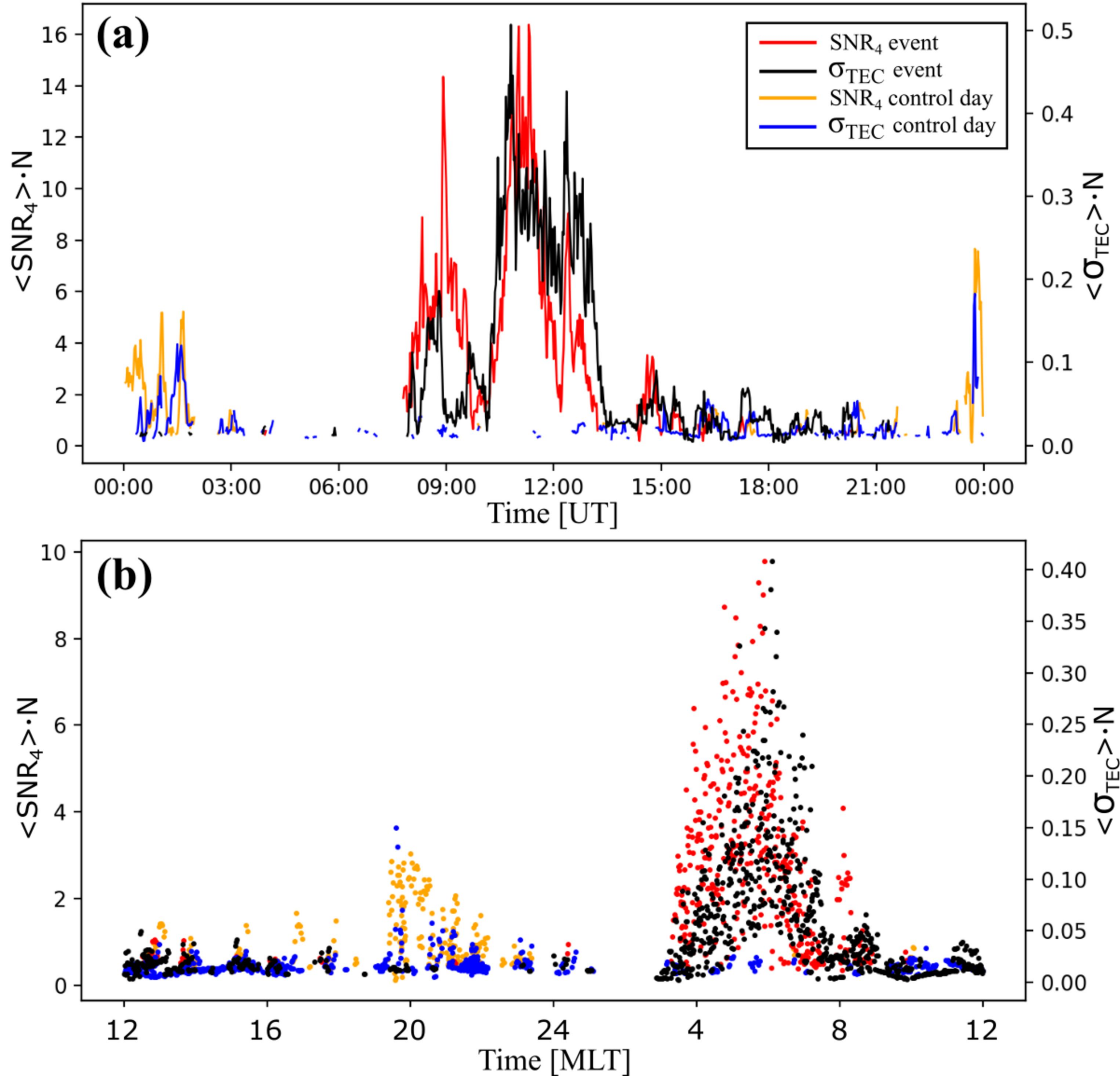
(a)
SNR4 event
σTEC event
SNR4 control day
σTEC control day
<SNR4>·N
<σTEC>·N
Time [UT]
00:00
03:00
06:00
09:00
12:00
15:00
18:00
21:00
00:00
(b)
<SNR4>·N
<σTEC>·N
Time [MLT]
12
16
20
24
4
8
12

Figure 4.

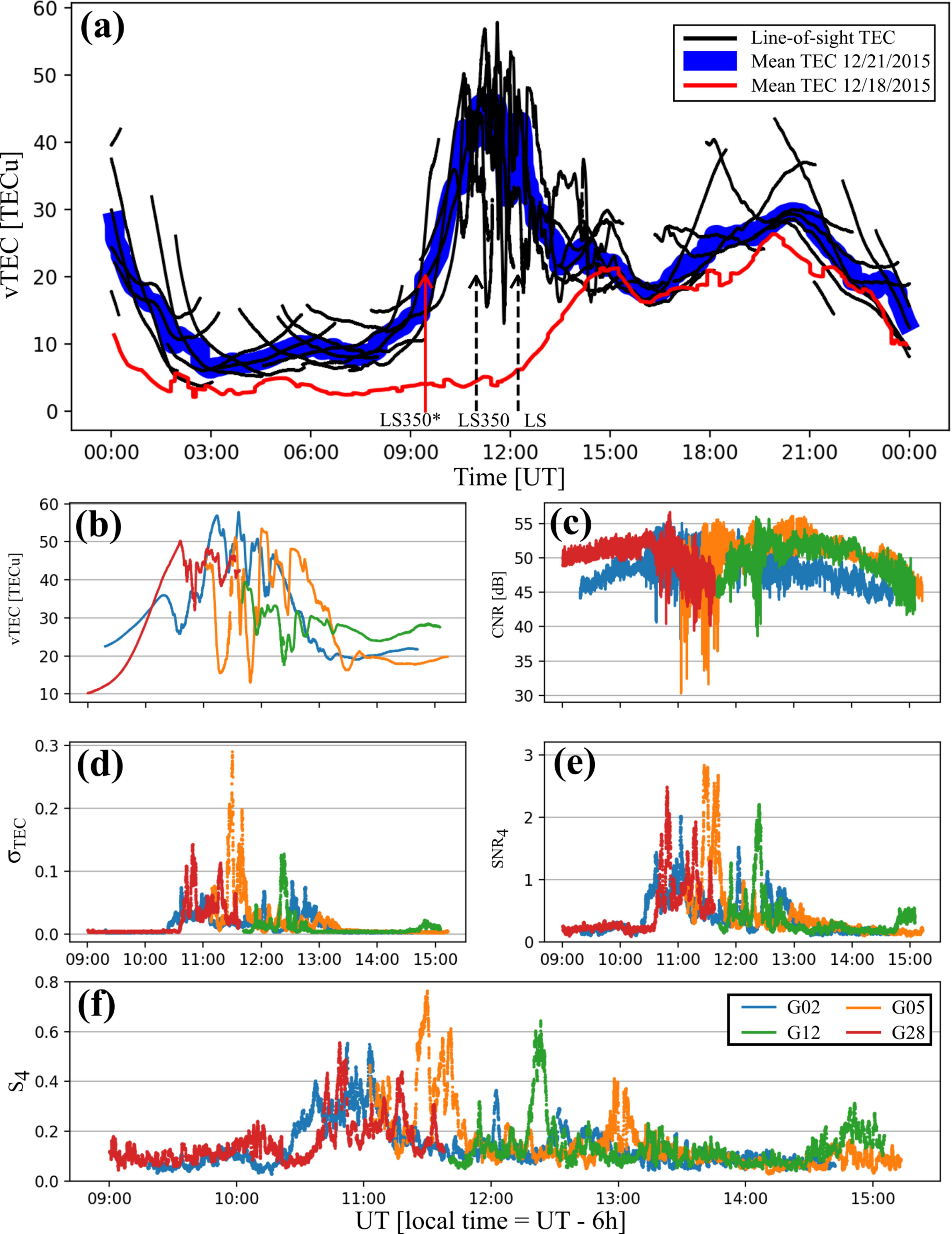

(a)
Line-of-sight TEC
Mean TEC 12/21/2015
Mean TEC 12/18/2015
vTEC [TECu]
LS350*
LS350
LS
Time [UT]
(b)
vTEC [TECu]
(c)
CNR [dB]
(d)
σ_{TEC}
(e)
SNR_4
(f)
S_4
G02
G05
G12
G28
UT [local time = UT - 6h]

Figure 5.

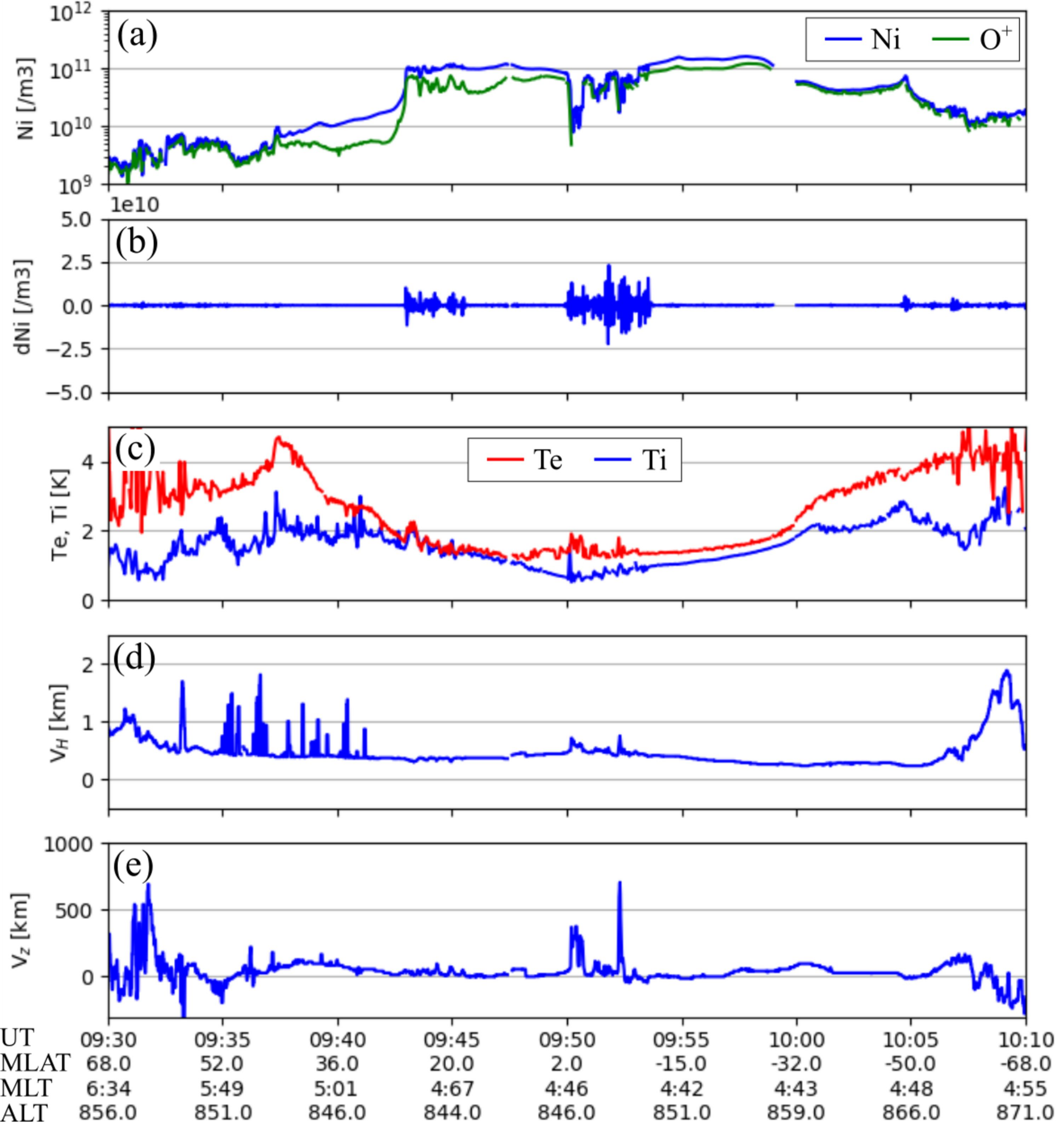

(a)
Ni
O+
Ni [/m3]
1e10
(b)
dNi [/m3]
(c)
Te
Ti
Te, Ti [K]
(d)
V_H [km]
(e)
V_z [km]
UT 09:30 09:35 09:40 09:45 09:50 09:55 10:00 10:05 10:10
MLAT 68.0 52.0 36.0 20.0 2.0 -15.0 -32.0 -50.0 -68.0
MLT 6:34 5:49 5:01 4:67 4:46 4:42 4:43 4:48 4:55
ALT 856.0 851.0 846.0 844.0 846.0 851.0 859.0 866.0 871.0